AGU PUBLICATIONS

Geophysical Research Letters

RESEARCH LETTER
10.1002/2014GL061796

Key Points:
- Seasonal Nordic Seas sea surface height variability
- Shelf waters are integral parts of the Nordic Seas circulation
- Eddy kinetic energy is dependent on the location of the sea ice edge

Supporting Information:
- Readme
- Figure S1
- Figure S2

Correspondence to:
S. Bacon,
s.bacon@noc.ac.uk

Citation:
Bulczak, A. I., S. Bacon, A. C. Naveira Garabato, A. Ridout, M. J. P. Sonnewald, and S. W. Laxon (2015), Seasonal variability of sea surface height in the coastal waters and deep basins of the Nordic Seas, *Geophys. Res. Lett.*, *42*, 113–120, doi:10.1002/2014GL061796.

Received 5 SEP 2014
Accepted 15 DEC 2014
Accepted article online 17 DEC 2014
Published online 12 JAN 2015

Seasonal variability of sea surface height in the coastal waters and deep basins of the Nordic Seas

Anna I. Bulczak[1,2], Sheldon Bacon[3], Alberto C. Naveira Garabato[1], Andrew Ridout[4], Maike J. P. Sonnewald[3,5], and Seymour W. Laxon[4,6]

[1]Ocean and Earth Science, University of Southampton, National Oceanography Centre, Southampton, UK, [2]Institute of Oceanology, Polish Academy of Sciences, Sopot, Poland, [3]National Oceanography Centre, Southampton, UK, [4]Centre for Polar Observation and Modelling, University College London, London, UK, [5]Institute for Complex Systems Simulation, University of Southampton, Southampton, UK, [6]Deceased 2 January 2013

Abstract Sea surface height measured by the Envisat radar altimeter over open ocean and from leads in sea ice are combined to generate a complete view of variability in the Nordic Seas, geographically and seasonally. The observed seasonal variability is decomposed using empirical orthogonal functions and is consistent with seasonal variations in steric and dynamic forcing. Wintertime increase in sea surface height on the east Greenland shelf is hypothesized to be caused by wind-forced downwelling, which provides direct evidence for the regional play of coastal dynamics. High levels of eddy kinetic energy around the sea ice edge in Fram Strait and off east Greenland and Svalbard are consistent with the interaction of the wind with the ice edge.

1. Introduction

The Nordic Seas are a curious part of the World Ocean. The high Arctic lies north of Fram Strait, and the Atlantic Ocean lies south of the Greenland-Scotland Ridge (see Figure 1a for regional nomenclature). Northward flowing Atlantic water fills the upper levels of the eastern part of the Nordic Seas, and some of the Atlantic water continues north into the high Arctic. In the western part, sea ice and freshened seawater of Arctic origin flow southward, supplemented by a recirculated fraction of Atlantic water. However, the Nordic Seas are far from being a passive conduit between these two major oceans. The release of heat from ocean to atmosphere impacts regional climate, and the dense waters formed in the Nordic Seas are a major constituent of the deep, south going limb of the Atlantic Meridional Overturning Circulation (AMOC). Additionally, the freshwater exported from the Arctic has the potential to modulate the strength of the AMOC. For an overview of the Nordic Seas, see *Mauritzen et al*. [2011].

Scientific measurements have been made in the Nordic Seas for over a century [e.g., *Knudsen*, 1899; *Helland-Hansen and Nansen*, 1909]. However, harsh weather conditions have meant that most measurements have been made in the summer, and mainly in the ice-free eastern part of the Nordic Seas. In the western part, knowledge of the mean circulation and its variability on time scales longer than a year is limited to Fram Strait [*De Steur et al*., 2009; *Beszczynska-Möller et al*., 2011], the Greenland Sea at 75°N [*Woodgate et al*., 1999], and Denmark Strait [*Macrander et al*., 2005]. Even during summer, the waters east of Greenland can be hard to access.

Two developments made remote-sensed (satellite) measurements useful in the whole of the Nordic Seas. First, the latitudinal limit of altimetry coverage was extended to 81.5°N with the European ERS and Envisat satellites. Second, *Peacock and Laxon* [2004] showed that altimetric measurements of the ocean sea surface height (SSH) could be used to study ocean circulation variability in the ice-covered part of the ocean by detection of radar energy reflected from leads (or other open water) in the sea ice. Previous publications have analyzed remote-sensed data over the open waters of the Nordic Seas. Our aim in this manuscript is to provide the first integral view of SSH variability over the whole of the Nordic Seas, and covering the whole of the seasonal cycle. We first describe data and methods (section 2), then results (section 3), discussion (section 4), and lastly final remarks (section 5).

2. Data and Methods

Along-track SSH measurements were acquired between November 2002 and October 2009 by the Envisat radar altimeter (RA-2). SSH from the open ocean was calculated using standard techniques; SSH from leads

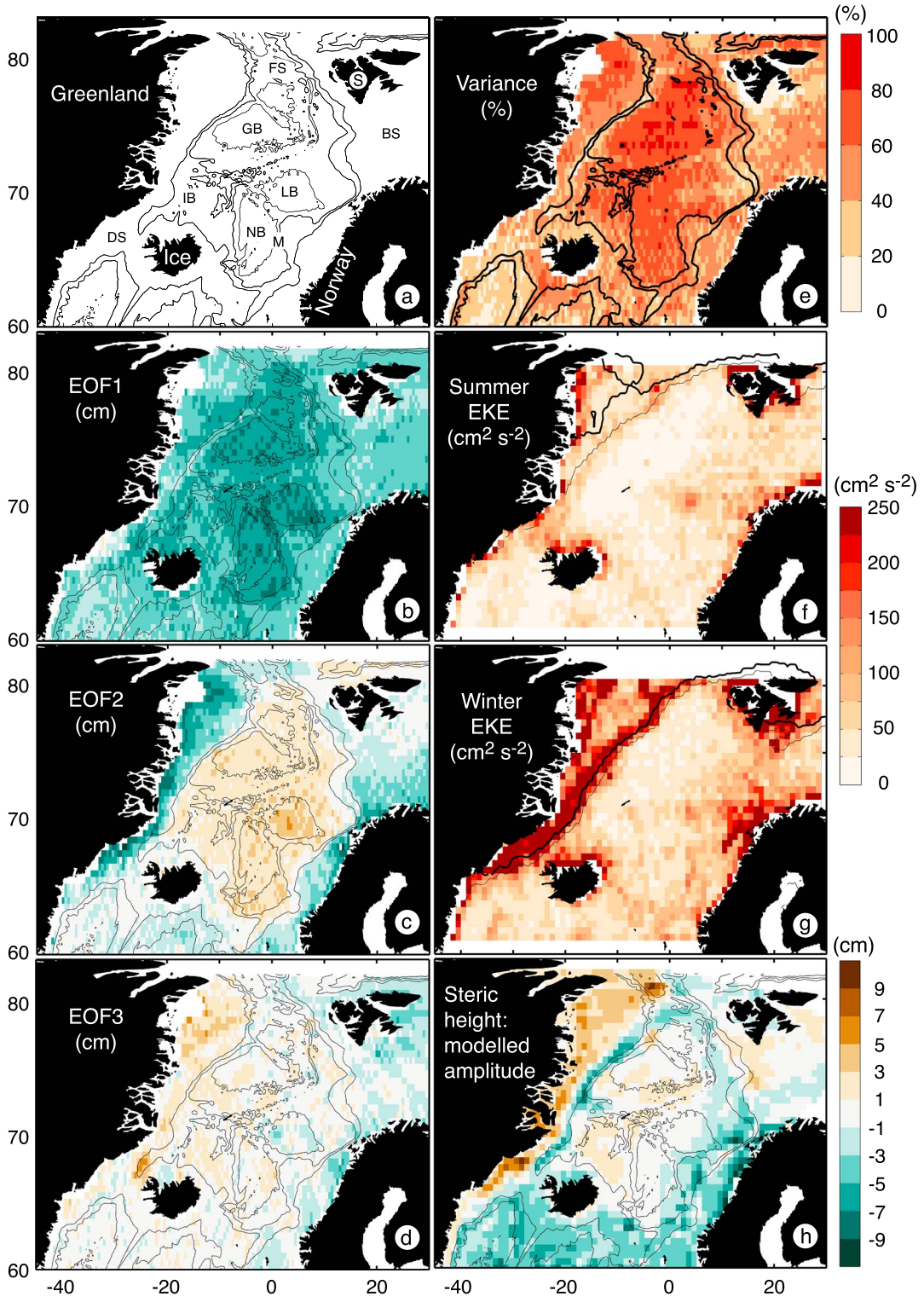

Figure 1. Regional nomenclature: (a) Fram Strait (FS), Denmark Strait (DS), Greenland Basin (GB), Iceland Basin (IB), Lofoten Basin (LB), Norwegian Basin (NB), Barents Sea (BS), Iceland (Ice), Svalbard (S), Ocean Weather Station Mike (M); the Greenland-Scotland Ridge is the shallow bathymetric feature connecting Greenland, Iceland, and Scotland (which is off the map to the south); depth contours are 1000, 2000, and 3000 m. (b) First, (c) second, and (d) third EOFs (cm). (e) Fraction of total SSH variance described by first three EOFs (%). (f) Summer and (g) winter EKE ($cm^2\ s^{-2}$). (h) Modeled steric height amplitude, calculated as summer minus winter, with regional average subtracted (cm).

within the ice-covered ocean was calculated using the method of *Peacock and Laxon* [2004]. There is a bias between elevation estimates from the open ocean and from leads because different models are used to fit to the altimeter return echoes to provide elevation estimates. The bias was calibrated using data from the ice edge (lead elevations are lower than ocean elevations); see *Giles et al.* [2012] (supporting information). The distribution of the bias (the difference between ocean and lead elevations) is approximately Gaussian with a mean, standard deviation, and standard error of 18, 10, and 0.2 cm, respectively, and there was no dependence of the bias with time or location [*Kaczmarska*, 2012]. We add the mean difference to the lead elevations to correct for this bias. The combined data set was generated by averaging onto a regular grid with spacing 0.5° in latitude and 1° in longitude at monthly intervals. Finally, for each grid point, the record time-mean (2002–2009) SSH was subtracted from the SSH to create the SSH anomaly (SSHA) data set. Figure S1 in the supporting information shows a summary of these data, presenting standard deviation of SSHA by season.

The key spatiotemporal patterns of variability of SSH in the Nordic Seas were determined using an Empirical Orthogonal Function (EOF) analysis, and the Monte Carlo method of *Overland and Preisendorfer* [1982] was used to determine the statistical significance of the EOF modes, whereby the autocorrelation time scale T is

$$T = \int_0^t a\left(t'\right)\, \mathrm{d}t' \tag{1}$$

where $a(t)$ is a mean autocorrelation function and t is the time needed for the function to reach zero. The effective number of degrees of freedom, D, was then calculated as $D = N/T$, where N is the length of the record, with $T = 1.7$ months and $N = 84$ months, $D = 50$.

To determine which EOFs are significant, and to assess the noise level of the SSHA data, one hundred sets of random, normally distributed data sets (with a mean of zero and standard deviation of one) of the same spatial size as the original SSHA data were generated, and the EOFs of those data sets were calculated. The temporal size of the random data had a dimension of the effective degrees of freedom. The obtained eigenvalues were then compared to the real eigenvalues of normalized SSHA. An EOF mode was significant at the 95% confidence level when its eigenvalue exceeds the eigenvalue of the randomly generated fields over 95% of the time. The results showed that the first three EOF modes were significant above the noise level of 2.4% of the total variance, or SSH variability below ~2 cm. The three significant modes account for 48.6% of the total variance. The method of *North et al.* [1982] was also applied as an independent check, with the same outcome: the first three EOFs are all significant.

A related metric of the variability in SSHA, often used in the discussion of the energetics of the ocean circulation and the dynamics of the oceanic mesoscale eddy field [*Ferrari and Wunsch*, 2009] is the surface eddy kinetic energy (EKE), calculated as $\mathrm{EKE} = (\langle u'^2 \rangle + \langle v'^2 \rangle)/2$. The zonal ($x$) and meridional ($y$) components of the surface geostrophic velocity are u and v, respectively, primes indicate anomalies from the mean, and angled brackets represent time averages. Velocity anomalies are calculated from the observed SSHA (η) as $u' = -(g/f)(\mathrm{d}\eta/\mathrm{d}y)$ and $v' = (g/f)(\mathrm{d}\eta/\mathrm{d}x)$, where f is the Coriolis parameter and g the gravitational acceleration. Prior to computing EKE, SSHA was mapped onto a 0.5° latitude × 1° longitude grid using a Gaussian weighting function with a horizontal half width of 60 km and a cutoff length scale of 100 km.

The Nucleus for European Modelling of the Ocean (NEMO) is a widely used framework for oceanographic modeling. The seasonal steric variation in the sea level of the Nordic Seas is assessed using NEMO. This approach provides complete geographical coverage throughout the calendar year, whereas measurements are completely lacking in some regions: particularly in winter under the seasonally ice-covered shelf waters. NEMO uses the primitive equation model Ocean Parallelisé 9.1 [*Madec and NEMO Team*, 2011] coupled with the Louvain-la-Neuve sea ice model (LIM2) [*Fichefet and Morales Maqueda*, 1997]. The model is discretized on a tripolar grid with two northern poles (one in Siberia, one in Canada) and the geographical South Pole. A detailed bathymetry is used by modification of the 2 min gridded global relief Earth Topography (ETOPO2v2). In the Nordic Seas, it contains *Smith and Sandwell* [1997] satellite data south of 72°N and the International Bathymetric Chart of the Arctic Ocean [*Jakobsson et al.*, 2008] north of 72°N. Description of ETOPO2v2 is available from the National Geophysical Data Center of the U.S. National Oceanic and Atmospheric Administration via their website at http://www.ngdc.noaa.gov/. Model atmospheric forcing is described by *Brodeau et al.* [2010]. Atmospheric features are drawn from the Common Ocean Reference Experiment 2 and the European Centre for Medium-Range Weather Forecasts. Air-sea and air-ice fluxes are calculated by atmospheric boundary layer

formulations [*Large and Yeager*, 2004]. Steric height calculations are conducted with monthly averaged model output. For comparability with the EOFs, we first calculated the summer-minus-winter steric height change in NEMO, then subtracted the area mean of this difference field (−4.5 cm), calculated north of 65°N, from the whole field.

Sea ice concentration data were downloaded from the U.S. National Snow and Ice Data Centre website at http://nsidc.org/data/nsidc-0051 [*Cavalieri et al*., 1996, updated yearly], for the area used in Figure 1, and for the same time span as Envisat.

3. Results

The first three EOFs are shown in Figure 1. EOF1 (Figure 1b) is a basin-wide, coherent "breathing" mode that explains 36% of the total variance. It shows the whole of the Nordic Seas (in relative terms) inflating and deflating with annual period. It is at a minimum in winter and maximum in summer. Its amplitude is lowest around the boundaries and over topography, and highest in the centers of the deep basins. EOF2 (Figure 1c) shows an antiphase relationship between the deep basins and the shelf waters off Norway and Greenland: when one is positive, the other is negative (and vice versa). The sign change occurs consistently close to the shelf edge, represented in Figure 1 by the 1000 m isobath. The on-shelf amplitude becomes larger toward the coast, while the deep basin amplitude increases (in the opposite sense) toward the centers of the deep basins. EOF2 explains 10% of the total variance, it oscillates with annual period, and it lags EOF1 by ~3 months (Figure S2). In EOF3 (Figure 1d), noise begins to emerge in the deep basins, evidenced by the appearance of structures related to the satellite ground tracks with amplitude ~2 cm. It explains only 3% of the total variance and shows a noisy annual cycle approximately in phase with EOF1, but as noted in section 2, it is still a significant EOF. Standing out from the background noise is the signal in the eastern and western shelf waters, with amplitude ~4 cm and opposite sign between east and west.

Figure 1e shows the geographical distribution of variance explained by the first three EOFs. They explain 49% of the total, and locally they explain: up to 90% in the Greenland and Norwegian basins; 60–70% in the Lofoten Basin, the Iceland Sea, the continental shelf off Northeast Greenland and off northern Svalbard; and 40–50% in the Barents Sea and the Norwegian continental shelf.

The distribution of EKE is shown for summer (Figure 1f) and winter (Figure 1g). It is high in several regions—notably so all along the East Greenland coast, following the continental shelf. There is enhancement toward the north of the Norwegian continental shelf, over the shallow waters south of Svalbard, and from the northwest to the east of Iceland. Two high-EKE features extend over deep water: one in the Lofoten Basin, and a second trending southwest to northeast from the Greenland shelf across Fram Strait.

4. Discussion

In this section, we hypothesize physical interpretations of the patterns of variability seen in the three leading EOFs and the EKE distribution.

To test whether EOF1 might show seasonal variability in steric height, we first inspected the best central basin records of year-round time series of temperature and salinity from surface to depth, from Ocean Weather Station Mike, located near 66°N, 2°E [*Nilsen and Falck*, 2006; *Skjelvan et al*., 2008]. The annual cycle amplitude of temperature is approximately 1–2°C over the upper ~300 m. Taking the coefficient of thermal expansion $\alpha \approx 1 \times 10^{-4} {}^{\circ}\mathrm{C}^{-1}$, the resulting amplitude of the thermal component of steric SSH variability is 2–4 cm. The (net) steric amplitude is similar to that of EOF1. To test this hypothesis further, we inspected NEMO model output, which was chosen for its complete coast-to-coast spatial coverage and unbiased temporal coverage. Its realism has been demonstrated in, e.g., *Bacon et al*. [2014]. Figure 1h shows the NEMO seasonal steric height amplitude. The mean amplitudes in both model and satellite data are similar, at ~5 cm. There is agreement both with the seasonal cycle amplitude of ~5 cm estimated by *Mork and Skagseth* [2005] and *Siegismund et al*. [2007] and also with their phase: their maximum steric height amplitudes occur around October, the same as ours (Figure S2).

However, the spatial patterns of EOF1 and model steric height amplitude are different. The model signal has maximum (highest negative) amplitude around the margins of the deep basins, following the paths of the major currents, and is more weakly negative in the centers of the deep basins. EOF1 generally increases from

low to high (negative) amplitude from the coastal margins, and also from the midbasin ridge systems, to the centers of the basins. The Nordic Seas experience (in the mean) cyclonic wind forcing [*Jonsson*, 1991; *Furevik and Nilsen*, 2005], and model experiments have shown that such forcing induces basin-scale and subbasin-scale circulation which follows bathymetric contours [*Nøst and Isachsen*, 2003; *Isachsen et al*., 2003]. *Voet et al*. [2010] use deep (1000–1500 m) float trajectories to calculate the seasonal cycles of deep velocities in the subbasins, which we use as proxies for barotropic velocities. The amplitudes of the cycles are greatest in the Norwegian and Greenland basins, at 1 and 1.5 cm s^{-1}, respectively, and weakest in the Iceland and Lofoten basins. EOF1 is qualitatively similar regarding the relative sizes of the SSH gradients across the four basins, and it is also quantitatively similar: for $\delta\eta \sim 3$ cm and a scale distance of 200 km, the resulting barotropic current variability is 1 cm s^{-1}. EOF1 shows a wintertime lowering (and vice versa in summertime) of SSH, and while this signal is likely to be mainly steric, it may also incorporate some element of seasonal dynamic variability.

EOF2 represents a contrast between the deep basins and the shelf waters of the Nordic Seas. In winter (November-December-January), SSH is a maximum on the shelves and a minimum in the deep basins (and vice versa in summer). The spatial pattern is consistent with a basin-wide response to wind forcing (Ekman pumping). EOF2 lags EOF1 by ~3 months; assuming that the timings of major seasonal changes in surface fluxes of heat and momentum are correlated, and expecting that heat flux changes will promote a fast steric response while the dynamic response to changes in wind forcing will be delayed, we next ask whether this is consistent with spin-up time scales (t_{spin}). *Gill* [1982] provides a simple expression (using an argument from Ekman pumping) to estimate t_{spin} for turbulent flows: $t_{spin} = H/(2C_D U)$. We set the drag coefficient $C_D = 10^{-3}$, typical depth $H = 3000$ m and velocity $U = 10$ cm s^{-1}, resulting in t_{spin} ~4 months. Also, *Isachsen et al*. [2003] obtain a spin-up time scale of 1–2 months. These are both broadly consistent with the observations.

The strongest surface current variability in EOF2 will result from the cross-shelf SSH gradient, particularly east of Greenland. Taking representative values of $\delta\eta \sim 5$ cm and a scale distance of 100 km, we find along-shelf current variability of ±4 cm s^{-1}, accelerating southward in winter and decelerating in summer. South of Denmark Strait, the East Greenland Coastal Current (EGCC) is known to exist on shelf all year [*Bacon et al*., 2014]. Their assessment of the EGCC near 63°N found a wind-driven component with seasonal variability ±8 cm s^{-1}, which may be consistent with the present observations.

The most significant signal in EOF3 is the late winter/early spring increase in SSH (Figure S2), by ~2 cm, east of Greenland. We suggest two possible causes. First, the explanation of EOF2 assumes synchronous air-sea momentum fluxes to both eastern and western shelf waters. An asynchronous component concentrated off east Greenland could produce the observed EOF3 response. Furthermore, it could be mediated by the seasonal loss (though melting and advection) of the local sea ice cover. Air-sea momentum fluxes are highest for high, but still mobile, concentrations of sea ice [*Tsamados et al*., 2014]; and average (northerly) winds off east Greenland are stronger than elsewhere in the Nordic Seas [*Furevik and Nilsen*, 2005].

The second possible explanation entails the cross-shelf circulation in the presence of downwelling favorable winds [*Moffat and Lentz*, 2012; *Bacon et al*., 2014]—northerlies off east Greenland [*Furevik and Nilsen*, 2005]. Ekman transport moves near-surface water shoreward, and the resulting bottom pressure gradient moves deep water offshore. Isopycnal tilt increases downward in the shoreward direction, so that near the coast, deeper, denser water is displaced by less dense water. Taking representative values from *Bacon et al*. [2014], the downward movement of isopycnals by ~100 m decreases salinity (S) by ~0.5. With density ρ, $\partial\rho/\partial S \approx -0.8$ kg m^{-3}, the resulting increase in SSH is 1 cm. The observed spatial pattern, meridional extent, and SSH amplitude are similar to the NEMO steric height change, so we favor the second explanation.

The distribution of EKE (Figures 1f and 1g) is strongly seasonal—high in winter, low in summer, which indicates a response to wind forcing. Furthermore, the spatial distribution of high EKE is congruent with low total variance explained by the first three EOFs (Figures 1b–1d), which indicates a (quasi-) stochastic process. We observe three geographical categories of EKE: open ocean, shelf/coastal, and ice edge, with some overlap between the latter two. We consider each in turn.

First, there is a persistent patch of high EKE in the Lofoten Basin centered near 3°E, 70°N, consistent with the "warm pool" formed by the coalescence of anticyclonic vortices originating at the Lofoten Escarpment, described in detail by *Rossby et al*. [2009] and *Koszalka et al*. [2011]. The low background levels of open ocean EKE are lower in the western basins than eastern, with the dividing line of the midbasin ridge system, indicative of greater instability in the north going Atlantic waters.

Second, the purely coastal/shelf EKE features, away from sea ice influence, appear in three places, and all likely derive from wind forcing and instability processes. North of Iceland, the variability is associated with the North Iceland Irminger Current [*Våge et al*., 2013]; off the coast of Norway, there is the Norwegian Coastal Current [*Haugan et al*., 1991; *Skagseth et al*., 2011] and the Lofoten eddy-shedding region [*Rossby et al*., 2009; *Koszalka et al*., 2011]; and west of Svalbard, the West Spitsbergen Current [*Teigen et al*., 2010, 2011].

Third, there is the Y-shaped feature east of Greenland seen in winter, where very high levels of EKE appear south of Denmark Strait and persist northward to ~75°N. Near this latitude, the southern end of the broad northeast Greenland shelf (Belgica Bank), the pattern divides. One branch remains close to the coast, and the other trends northeastward, initially following the shelf break but then crossing Fram Strait toward Svalbard. Instability processes are known to generate eddies which contribute to the recirculation of Atlantic water in the vicinity of Fram Strait [*Teigen et al*., 2010, 2011], and the East Greenland Current (EGC) flowing south down the shelf break is eddy rich [*Woodgate et al*., 1999]. Winds generate eddies at the ice edge [*Johannessen et al*., 1983, 1987], and EGC eddies and their relationship to the ice edge are illustrated by *Zhang et al*., 2011. The position of the ice edge relative to the shelf break exerts control over wind-driven upwelling and downwelling [*Carmack and Chapman*, 2003], and winds favoring downwelling at the ice edge will generate eddies because downwelling jets are unstable [*Häkkinen*, 1986]. Furthermore, on-shelf SSH variations on short time scales will result from wind forcing variability [*Lentz*, 2004; *Moffat and Lentz*, 2012], and the winds off Greenland near Denmark Strait (barrier winds) can be strong and highly variable [*Moore and Renfrew*, 2005]. The EKE band east of Greenland is therefore likely to derive from the complex interplay of ice, ocean, coast, bathymetry, and winds, and these arguments should also apply to the patch of variability southeast of Svalbard. *Heorton et al*. [2014] model the response of sea ice edge regions to atmospheric and oceanic jet formation. There is a remarkable similarity between our EKE results and their locations and relative intensities of jet formation (their Figures 12a and 12b), and there is a very close match in winter between the location of the ice edge and of the EKE maxima, both east of Greenland and south and east of Svalbard (Figure 1g).

5. Final Remarks

We have provided the first integral view of SSH variability over the whole of the Nordic Seas, including ice-covered regions, and spanning all seasons. The annual cycle is a major component of the variability across the Nordic Seas. The coherent component is partly the steric response to seasonal temperature change, and partly dynamic, resulting from seasonal spin-up/spin-down of the Nordic Seas circulation. The shelf waters are an important element of the dynamic variability. The stochastic component illustrates the widespread importance of eddies in the region and their seasonal variability.

We have described our interpretations of the variability in SSH, but more work is needed to confirm these interpretations and to elucidate their importance. We speculate here on one potential impact of future changes. Arctic sea ice thickness and extent is predicted to continue to decline [*Intergovernmental Panel on Climate Change*, 2013]. Mixing (induced by eddies) along the EGC in the Nordic Seas sets the properties of the intermediate waters that form the Denmark Strait Overflow [*Strass et al*., 1993], which is one of the primary components of the deep, south going limb of the AMOC [*Dickson and Brown*, 1994]. If eddy formation is tied to ice edge processes, then perhaps the properties and transports of the Overflow will change in future, with consequences for the AMOC.

Acknowledgments
Data of raw SSH and atmospheric corrections were obtained directly from the European Space Agency (WAP data, level 0) and processed at CPOM (UCL). This study was funded by the UK Natural Environment Research Council and is a contribution to the TEA-COSI project (NE/I028947/1).

The Editor thanks two anonymous reviewers for their assistance in evaluating this paper.

References

Bacon, S., A. Marshall, N. P. Holliday, Y. Aksenov, and S. R. Dye (2014), Seasonal variability of the East Greenland coastal current, *J. Geophys. Res. Oceans*, *119*, doi:10.1002/2013JC009279.

Beszczynska-Möller, A., E. Fahrbach, U. Schauer, and E. Hansen (2011), Variability in Atlantic water temperature and transport at the entrance to the Arctic Ocean, 1997–2010, *ICES J. Mar. Sci.*, *69*, 852–863, doi:10.1093/icesjms/fss056.

Brodeau, L., B. Barnier, A.-M. Treguier, T. Penduff, and S. Gulev (2010), An ERA40-based atmospheric forcing for global ocean circulation models, *Ocean Model.*, *31*, 88–104, doi:10.1016/j.ocemod.2009.10.005.

Carmack, E., and D. C. Chapman (2003), Wind-driven shelf/basin exchange on an Arctic shelf: The joint roles of ice cover extent and shelf-break bathymetry, *Geophys. Res. Lett.*, *30*(14), 1778, doi:10.1029/2003GL017526.

Cavalieri, D. J., C. L. Parkinson, P. Gloersen, and H. Zwally (1996, updated yearly), Sea Ice Concentrations from Nimbus-7 SMMR and DMSP SSM/I-SSMIS Passive Microwave Data, [2002–2009, 60–85°N, 50°W–30°E], NASA DAAC at the National Snow and Ice Data Center, Boulder, Colo.

De Steur, L., E. Hansen, R. Gerdes, M. Karcher, E. Fahrbach, and J. Holfort (2009), Freshwater fluxes in the East Greenland Current: A decade of observations, *Geophys. Res. Lett.*, *36*, L23611, doi:10.1029/2009GL041278.

Dickson, R. R., and J. Brown (1994), The production of North Atlantic deep water: Sources, rates, and pathways, *J. Geophys. Res.*, *99*, 12,319–12,341, doi:10.1029/94JC00530.
Ferrari, R., and C. Wunsch (2009), Ocean circulation kinetic energy: Reservoirs sources, and sinks, *Annu. Rev. Fluid Mech.*, *41*, 253–282, doi:10.1146/annurev.fluid.40.111406.102139.
Fichefet, T., and M. Morales Maqueda (1997), Sensitivity of a global sea ice model to the treatment of ice thermodynamics and dynamics, *J. Geophys. Res.*, *102*, 12,609–12,646, doi:10.1029/97JC00480.
Furevik, T., and J. E. Ø. Nilsen (2005), Large-scale atmospheric circulation variability and its impacts on the Nordic Seas ocean climate: A review, in *The Nordic Seas: An Integrated Perspective, Geophys. Monogr. Ser*, vol. 158, edited by H. Drange et al., pp. 105–136, AGU, Washington, D. C.
Giles, K. A., S. W. Laxon, A. L. Ridout, D. J. Wingham, and S. Bacon (2012), Western Arctic Ocean freshwater storage increased by wind-driven spin-up of the Beaufort Gyre, *Nat. Geosci.*, *5*, 194–197, doi:10.1038/NGEO1379.
Gill, A. E. (1982), *Atmosphere–Ocean Dynamics*, Academic Press, London.
Häkkinen, S. (1986), Coupled ice-ocean dynamics in the marginal ice zones: Upwelling/downwelling and eddy generation, *J. Geophys. Res.*, *91*(C1), 819–832, doi:10.1029/JC091iC01p00819.
Haugan, P. M., G. Evensen, J. A. Johannessen, O. M. Johannessen, and L. H. Pettersson (1991), Modeled and observed mesoscale circulation and wave-current refraction during the 1988 Norwegian Continental Shelf Experiment, *J. Geophys. Res.*, *96*, 10,487–10,506, doi:10.1029/91JC00299.
Helland-Hansen, B., and F. Nansen (1909), The Norwegian Sea: Its physical oceanography based upon the Norwegian researches 1900–1904, *Rep. Norwegian Fish. Mar. Invest.*, *2*(2), 1–390.
Heorton, H., D. Feltham, and J. Hunt (2014), The response of the sea ice edge to atmospheric and oceanic jet formation, *J. Phys. Oceanogr.*, *44*, 2292–2316, doi:10.1175/JPOD-13-0184.1.
Intergovernmental Panel on Climate Change (2013), Climate Change 2013: The Physical Science Basis, in *Contribution of Working Group I to the Fifth Assessment Report of the Intergovernmental Panel on Climate Change*, edited by T. F. Stocker et al., 1535 pp., Cambridge Univ. Press, Cambridge, U. K., and New York.
Isachsen, P. E., J. H. LaCasce, and C. Mauritzen (2003), Wind-driven variability of the large-scale recirculating flow in the Nordic Seas and Arctic Ocean, *J. Phys. Oceanogr.*, *33*, 2534–2550.
Jakobsson, M., R. Macnab, L. Mayer, R. Anderson, M. Edwards, J. Hatzky, H. W. Schenke, and P. Johnson (2008), An improved bathymetric portrayal of the Arctic Ocean: Implications for ocean modeling and geological, geophysical and oceanographic analyses, *Geophys. Res. Lett.*, *35*, L07602, doi:10.1029/2008GL033520.
Johannessen, J. A., et al. (1987), Mesoscale eddies in the Fram Strait marginal ice zone during the 1983 and 1984 marginal ice zone experiments, *J. Geophys. Res.*, *92*, 6754–6772, doi:10.1029/JC092iC07p06754.
Johannessen, O. M., J. A. Johannessen, J. Morison, B. A. Farrelly, and E. A. S. Svendsen (1983), Oceanographic conditions in the marginal ice zone north of Svalbard in early fall 1979 with an emphasis on mesoscale processes, *J. Geophys. Res.*, *88*, 2755–2769, doi:10.1029/JC088iC05p02755.
Jonsson, S. (1991), Seasonal and interannual variability of wind stress curl over the Nordic Seas, *J. Geophys. Res.*, *96*, 2694–2659.
Kaczmarska, A. I. (2012), Seasonal and interannual sea surface height variability in the Nordic Seas, PhD thesis, Univ. of Southampton, Southampton, U. K.
Knudsen, M. (1899), Hydrography, in *The Danish Ingolf Expedition*, vol. 1, pp. 23–161, Bianco Luno, Copenhagen.
Koszalka, I., J. H. LaCasce, M. Andersson, K. A. Orvik, and C. Mauritzen (2011), Surface circulation in the Nordic Seas from clustered drifters, *Deep Sea Res., Part I*, *58*, 468–485, doi:10.1016/j.dsr.2011.01.007.
Large, W. G., and S. G. Yeager (2004), Diurnal to decadal global forcing for ocean and sea-ice models: The data sets and flux climatologies, *Tech. Note NCAR/TN-460 + STR*, Natl. Cent. for Atmos. Res., Boulder, Colo.
Lentz, S. (2004), The response of buoyant coastal plumes to upwelling-favorable winds, *J. Phys. Oceanogr.*, *34*, 2458–2469.
Macrander, A., U. Send, H. Valdimarsson, S. Jonsson, and R. H. Käse (2005), Interannual changes in the overflow from the Nordic Seas into the Atlantic Ocean through Denmark Strait, *Geophys. Res. Lett.*, *32*, L06606, doi:10.1029/2004GL021463.
Madec, G., and NEMO Team (2011), NEMO Ocean Engine, Version 3.3, *Note du Pole de Modelisation*, Inst. Pierre-Simon Laplace, Paris.
Mauritzen, C., et al. (2011), Closing the loop—Approaches to monitoring the state of the Arctic Mediterranean during the International Polar Year 2007–2008, *Prog. Oceanogr.*, *90*, 62–89, doi:10.1016/j.pocean.2011.02.010.
Moffat, C., and S. Lentz (2012), On the response of a buoyant plume to downwelling-favorable wind stress, *J. Phys. Oceanogr.*, *42*, 1083–1098, doi:10.1175/JPO-D-11-015.1.
Moore, G. W. K., and I. A. Renfrew (2005), Tip jets and barrier winds: A QuikSCAT climatology of high wind speed events around Greenland, *J. Clim.*, *18*, 3713–3725, doi:10.1175/JCLI3455.1.
Mork, K. A., and Ø. Skagseth (2005), Annual sea surface height variability in The Nordic Seas, in *The Nordic Seas: An Integrated Perspective, Geophys. Monogr. Ser*, vol. 158, edited by H. Drange et al., pp. 51–64, AGU, Washington, D. C.
Nilsen, J. E. Ø., and E. Falck (2006), Variations of mixed layer properties in the Norwegian Sea for the period 1948–1999, *Prog. Oceanogr.*, *70*, 58–90, doi:10.1016/j.pocean.2006.03.014.
North, G. R., T. L. Bell, R. F. Calahan, and F. J. Moeng (1982), Sampling errors in the estimation of empirical orthogonal functions, *Mon. Weather Rev.*, *110*, 699–706.
Nøst, O. A., and P. E. Isachsen (2003), The large-scale time-mean ocean circulation in the Nordic Seas and the Arctic Ocean estimated from simplified dynamics, *J. Mar. Res.*, *61*, 175–210.
Overland, J. E., and R. Preisendorfer (1982), A significance test for principal components applied to a cyclone climatology, *Mon. Weather Rev.*, *110*, 1–4.
Peacock, N. R., and S. W. Laxon (2004), Sea surface determination in the Arctic Ocean from ERS altimetry, *J. Geophys. Res.*, *109*, C07001, doi:10.1029/2001JC001026.
Rossby, T., V. Ozhigin, V. Ivshin, and S. Bacon (2009), An isopycnal view of the Nordic Seas hydrography with focus on properties of the Lofoten Basin, *Deep Sea Res., Part I*, *56*, 1955–1971, doi:10.1016/j.dsr.2009.07.005.
Siegismund, F., J. Johannessen, H. Drange, K. A. Mork, and A. Korablev (2007), Steric height variability in the Nordic Seas, *J. Geophys. Res.*, *112*, C12010, doi:10.1029/2007JC004221.
Skagseth, Ø., K. F. Drinkwater, and E. Terrile (2011), Wind- and buoyancy-induced transport of the Norwegian coastal current in the Barents Sea, *J. Geophys. Res.*, *116*, C08007, doi:10.1029/2011JC006996.
Skjelvan, I., E. Falck, F. Rey, and S. B. Kringstad (2008), Inorganic carbon time series at ocean weather station Mike in the Norwegian Sea, *Biogeosciences*, *5*, 549–560, doi:10.5194/bg-5-549-2008.
Smith, W. H. F., and D. T. Sandwell (1997), Global sea floor topography from satellite altimetry and ship depth soundings, *Science*, *277*, 1956–1962.
Strass, V. H., E. Fahrbach, U. Schauer, and L. Sellmann (1993), Formation of Denmark Strait overflow water by mixing in the East Greenland Current, *J. Geophys. Res.*, *98*, 6907–6919, doi:10.1029/92JC02732.

Teigen, S. H., F. Nilsen, and B. Gjevik (2010), Barotropic instability in the West Spitsbergen Current, *J. Geophys. Res.*, *115*, C07016, doi:10.1029/2009JC005996.

Teigen, S. H., F. Nilsen, R. Skogseth, B. Gjevik, and A. Beszczynska-Möller (2011), Baroclinic instability in the West Spitsbergen Current, *J. Geophys. Res.*, *116*, C07012, doi:10.1029/2011JC006974.

Tsamados, M., D. L. Feltham, D. Schroeder, D. Flocco, S. L. Farrell, N. Kurtz, S. W. Laxon, and S. Bacon (2014), Impact of variable atmospheric and oceanic form drag on simulations of Arctic sea ice, *J. Phys. Oceanogr.*, *44*, 1329–1353, doi:10.1175/JPO-D-13-0215.1.

Våge, K., R. S. Pickart, M. A. Spall, G. W. K. Moore, H. Valdimarsson, D. J. Torres, S. Y. Erofeeva, and J. E. Ø. Nilsen (2013), Revised circulation scheme north of Denmark Strait, *Deep Sea Res., Part I*, *79*, 20–39, doi:10.1016/j.dsr.2013.05.007.

Voet, G., D. Quadfasel, K. A. Mork, and H. Søiland (2010), The mid-depth circulation of the Nordic Seas derived from profiling float observations, *Tellus A*, *62*, 516–529, doi:10.1111/j.1600-0870.2010.00444.x.

Woodgate, R. A., E. Fahrbach, and G. Rohardt (1999), Structure and transports of the East Greenland Current at 75°N from moored current meters, *J. Geophys. Res.*, *104*, 18,059–18,072, doi:10.1029/1999JC900146.

Zhang, R., T. L. Delworth, A. Rosati, W. G. Anderson, K. W. Dixon, H.-C. Lee, and F. Zeng (2011), Sensitivity of the North Atlantic Ocean circulation to an abrupt change in the Nordic Sea overflow in a high resolution global coupled climate model, *J. Geophys. Res.*, *116*, C12024, doi:10.1029/2011JC007240.